Ray-Based Modeling of Cross-Beam Energy Transfer at Caustics

In laser-based inertial confinement fusion (ICF), a millimeter-scale cryogenic capsule of deuterium–tritium fuel with a thin outer ablator is imploded either directly by laser illumination or indirectly by x rays emitted from a laser-heated, high-Z hohlraum.[1,2] In both approaches, multiple laser beams overlap in a plasma and their low-frequency beat waves can drive ion-acoustic waves. By means of a process known as cross-beam energy transfer (CBET), the ion-acoustic waves mediate the transfer of energy between beams, significantly impacting the deposition of laser energy.[3]

Direct-drive ICF experiments on the OMEGA laser[4] have shown a 10% to 20% reduction in laser absorption because of CBET.[5] Indirect-drive ICF experiments at the National Ignition Facility (NIF) have exploited CBET to control implosion symmetry by tuning the wavelength separation between laser beams.[6,7] The scale of these experiments, in terms of preparation time, complexity, and cost, necessitate the use of radiation-hydrodynamic simulations with CBET models for the rapid design, tuning, and optimization of implosions.[8]

As a result of the computational expense of wave-based calculations, the CBET models used in radiation-hydrodynamic codes are exclusively based on ray tracing; even then, 3-D implementations can be prohibitive. Furthermore, existing CBET models require artificial multipliers to obtain quantitative agreement with experiments.[7,9–12] This is, in part, due to a major challenge of ray tracing: the reconstruction of the field amplitude diverges at caustics. While sophisticated techniques exist for approximating the full solution to the electromagnetic wave equation in the vicinity of caustics,[13] there is no consensus as to how caustics should be treated in ray-based CBET models.

The use of artificial multipliers is particularly problematic in the complex radiation-hydrodynamic codes used to simulate ICF implosions because they model the interaction between many different physical processes, and an artificial multiplier in one physics model can mask deficiencies and inhibit progress in seemingly unrelated areas. Similarly, it is important to validate reduced models like ray-based CBET calculations against more-complete calculations so that when discrepancies do arise, there is some level of confidence as to whether the discrepancy is caused by missing physics or an inaccurate solution to the original problem.

In this article, we present a ray-based CBET algorithm that opens up the possibility for full-scale 3-D CBET modeling in radiation-hydrodynamic codes without the need for artificial multipliers. The key insight is that the energy transfer between beams should be truncated past the caustic of the pump beam. Ray-based CBET calculations with caustic gain truncation (CGT) show excellent agreement with laser absorption from both 2-D wave-based calculations and a 3-D 60-beam OMEGA implosion. A large difference between results obtained with and without CGT (in terms of both accuracy and energy conservation) indicates the importance of including a careful treatment of caustics in ray-based CBET calculations.

Ray-based CBET modeling relies on the assumption that the energy exchange between two lasers can be approximated locally using the homogeneous gain, and that the interaction between all rays in a given region of space can be treated independently, pairwise. Additionally, the large separation between the hydrodynamic and acoustic/electromagnetic time scales allows for steady-state CBET calculations using the instantaneous hydrodynamic conditions.

The general approach to ray-based CBET modeling follows four steps: (1) calculate trajectories for all rays in each laser beam, (2) discretize the ray trajectories along their paths, (3) determine all possible pairwise interactions, and (4) solve the resulting system of equations for the energies along the ray paths. Here it is assumed that steps (1) and (2) have already been completed. In terms of the absolute square of the enveloped electric field, the differential change of the ith ray (the seed ray) at the jth location along its path resulting from an interaction with the kth ray (the pump ray) at the lth location along its path for parallel-polarized beams in a homogeneous plasma is (in cgs units)[3]

$$\frac{d\left|E_{ij}\right|^2}{ds} = -\frac{\left|E_{ij}\right|^2}{L_a^{ij}} + \frac{g_{ijkl}}{L_s^{ijkl}}\frac{\left|E_{ij}\right|^2}{\sqrt{\varepsilon}}\frac{\left|E_{kl}\right|^2}{\left|E_{k0}\right|^2}, \quad (1)$$

where $\varepsilon = 1 - n_e/n_c$, n_e is the electron density,

$$n_c = m_e\omega_{ij}^2/\left(4\pi e^2\right)$$

is the critical density for light with frequency ω_{ij} (and wave vector $\mathbf{k}_{ij}$), m_e is the electron mass, $-e$ is the electron charge,

$$\left(L_s^{ijkl}\right)^{-1} = \frac{e^2\left|E_{k0}\right|^2}{4m_e c\omega_{ij}k_B T_e\left(1 + 3T_e/ZT_e\right)}\frac{n_e}{n_c}\frac{\omega_s}{\nu_{ia}}P\left(\eta_{ijkl}\right),$$

$$P(\eta) = \frac{\left(\nu_{ia}/\omega_s\right)^2\eta}{\left(\eta^2 - 1\right)^2 + \left(\nu_{ia}/\omega_s\right)^2\eta^2},$$

$$\eta_{ijkl} = \frac{\omega_{kl} - \omega_{ij} - \left(\mathbf{k}_{kl} - \mathbf{k}_{ij}\right)\cdot\mathbf{u}}{\omega_s},$$

ν_{ia} is the ion-acoustic wave energy–damping rate, ω_s is the acoustic frequency, T_e (T_i) is the electron (ion) temperature, Z is the ionization state, k_B is Boltzmann's constant, and $\mathbf{u}$ is the plasma flow velocity. $L_a^{ij} = c\sqrt{\varepsilon}\, n_c/\left(\nu_{ei}n_e\right)$ is the laser absorption length,[14] where

$$\nu_{ei} = 4\sqrt{2\pi}\, e^4 Z^2 n_i \Lambda_{ei}/\left(3\sqrt{m_e}\, T_e^{3/2}\right);$$

Λ_{ei} is the Coulomb logarithm;[15] $\left|E_{k0}\right| = \sqrt{8\pi I_{k0}/c}$ is the magnitude of the incident (vacuum) field of the kth ray; and I_{k0} is the corresponding intensity.

The function g_{ijkl} is introduced to account for the fact that there may not be a valid interaction between the two rays. Two rays will interact if they (1) intersect in configuration space and (2) are on distinct "sheets," where each sheet corresponds to a region of ray phase space that has a single-valued projection onto the configuration space [the divisions between sheets are at caustics (shown later in Fig. 155.8)].[13] Accordingly, $g_{ijkl} = 1$ if both of these conditions are satisfied and 0 otherwise. If the ray paths are discretized on a grid, being at the same location in configuration space is equivalent to being in the same grid cell.

Equation (1) can be discretized along ray trajectories in an inhomogeneous plasma if it is written in terms of ray energy, which is conserved along ray trajectories in the absence of CBET and absorption. In the geometric optics limit, $\left|E_{ij}\right|^2/\left|E_{i0}\right|^2 = W_{ij}\left(dS_{i0}/dS_{ij}\right)/\sqrt{\varepsilon}$, where W_{ij} is the ray energy normalized to the incident energy ($W_{i0} = 1$) and dS_{i0}/dS_{ij} is the ratio of the initial to current cross-sectional area of the ith ray, which is tracked by tracing bundles of rays.[16] This approximation for the fields diverges at caustics where either $\varepsilon \to 0$ or $dS_{ij}/dS_{i0} \to 0$. A simple way to correct for this is to treat the density profile as being locally linear. The field of a plane wave incident on a linear density gradient $\left(n_e/n_c = x/L\right)$ has an analytic solution (Airy function) with a peak field

$$\left(\left|E_{ij}\right|^2/\left|E_{i0}\right|^2\right)_{max} = \xi_{ij}\left(n_e/n_c\right)_{i,max}^{1/2}$$

(Ref. 14), where $\left(n_e/n_c\right)_{i,max}$ is the maximum density along the path of the ith ray, $\xi_{ij} = 0.9\left(\omega_{ij}L/c\right)^{1/3}$, and $L = L_*n_c/n_*$ (n_* and L_* are the density and density scale length at the caustic). Applying this as a limit to the peak field amplitude, Eq. (1) becomes

$$\frac{dW_{ij}}{ds} = -\frac{W_{ij}}{L_a^{ij}} + g_{ijkl}\frac{W_{ij}W_{kl}}{\sqrt{\varepsilon}\, L_s^{ijkl}}\min\left[\frac{1}{\sqrt{\varepsilon}}\frac{dS_{k0}}{dS_{kl}}, \xi_{kl}\left(\frac{n_e}{n_c}\right)_{max}^{1/2}\right]. \quad (2)$$

Equation (2) is the differential change in energy caused by a single pairwise interaction. In general, each ray can interact with every other sheet at every point along its path. Discretizing Eq. (2) along the ray paths and summing over all possible interactions gives

$$\frac{W_{i,j+1}}{W_{ij}} = \exp\left(-\frac{s_{ij}}{L_a^{ij}} + \frac{s_{ij}}{\sqrt{\varepsilon_{eff}}}\sum_{\mathscr{S}}\sum_{kl\in\mathscr{S}}\frac{W_{kl}g_{ijkl}\Delta S_{kl}}{\sum_{np\in\mathscr{S}}g_{ijnp}}\right), \quad (3)$$

where

$$\frac{1}{\sqrt{\varepsilon_{eff}}} = \min\left(\frac{1}{\sqrt{\varepsilon}}, 2\sqrt{\frac{L}{s_{ij}}}\right),$$

$$\Delta S_{kl} = \min\left[\frac{1}{\sqrt{\varepsilon}}\frac{dS_{k0}}{dS_{kl}}, \xi_{kl}\left(\frac{n_e}{n_c}\right)_{max}^{1/2}\right],$$

and s_{ij} is the length of the ray-path section from j to $j + 1$ for ray i. ε_{eff} is introduced to keep the discretized equation from diverging when $\varepsilon \to 0$, which originates from the vanishing group velocity of the seed beam for near-normal-incidence rays. The path integral is finite, so we use the analytic result for normal-incidence rays in a linear density gradient,

$$\int_{L-s}^{L} dx / \sqrt{1 - x/L} = 2\sqrt{sL}.$$

The first sum in Eq. (3) is over sheets $\mathscr{S}$, and the second sum is over all of the ray-path locations belonging to sheet $\mathscr{S}$. The summand corresponds to the expected interaction strength from all of the rays in the current grid cell on the current pump-beam sheet. In practice, it is more efficient if just one nonzero term from each sheet is used (chosen randomly). This has essentially no impact on the solution because all of the terms in the sums over k,l are equal in the limit $s_{ij} \to 0$.

Equation (3) is typically solved using fixed-point iteration. To improve the rate of convergence,[16] we substitute $\tilde{W}_{ij} \equiv W_{ij} / W_{i,j-1}$ and obtain the ray-based CBET equation

$$\tilde{W}_{i,j+1} = \exp\left(-A_{ij} + \sum_{\mathscr{S}} \sum_{kl \in \mathscr{S}} G_{ijkl} \prod_{m=1}^{l} \tilde{W}_{km}\right), \quad (4)$$

where

$$G_{ijkl} = \frac{s_{ij} g_{ijkl} \Delta S_{kl}}{\sqrt{\varepsilon_{eff}} L_s^{ijkl} \sum_{np \in \mathscr{S}} g_{ijnp}} \quad (5)$$

and $A_{ij} = s_{ij} / L_a^{ij}$. Equation (4) is written in the form that is used to solve for $\tilde{W}_{ij}$ because the A_{ij} and G_{ijkl} can be precalculated before starting the iterations. After solving for $\tilde{W}_{ij}$, the normalized ray energies are given by $\tilde{W}_{ij} = \prod_{k=1}^{j} \tilde{W}_{ik}$. Here the rays were discretized on a Cartesian grid except for the special case of rays changing sheets in a grid cell, where an additional split in the ray path is introduced at the sheet boundary. The limitations of this model that require the introduction of CGT are best illustrated by first introducing a prototypical example of CBET in the presence of fold caustics.

Figure 155.6 compares the electric fields from 2-D (a) ray- and (b) wave-based calculations of CBET between two beams in an azimuthally symmetric plasma. The wave-based calculations were performed using *LPSE* (laser–plasma simulation environment).[16,17] The ray-based solution was obtained by solving Eq. (4) and then taking the coherent sum of the fields from the four ray sheets (two from each beam).[13] The plasma conditions were similar to what would be encountered in an OMEGA implosion except they have been scaled down by a factor of 4. The laser intensities were 2×10^{15} W/cm^2 (0.351-μm light), which was chosen such that CBET would have a significant impact on the laser-energy deposition. The *LPSE* grid resolution was 50 cells/μm. The fact that the results from the two calculations are difficult to distinguish by eye is a testament to the fact that the geometric optics approximation is valid
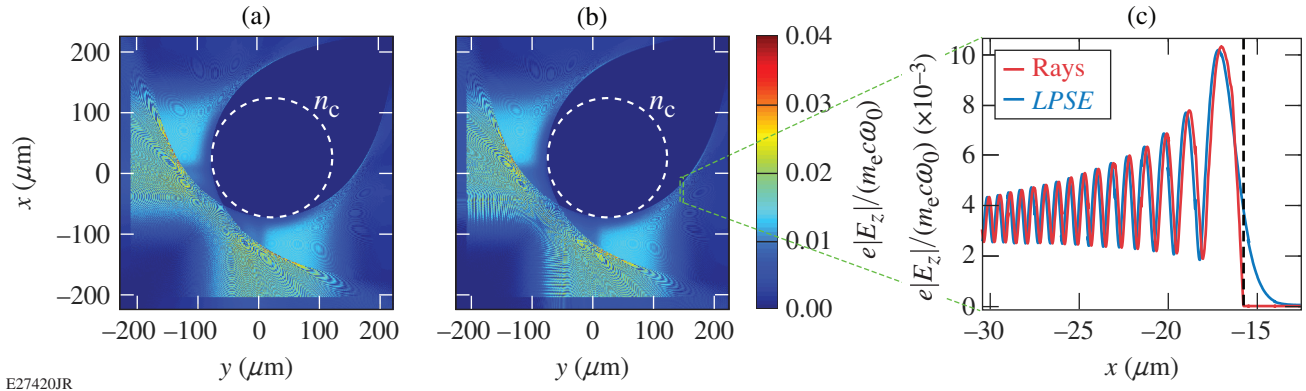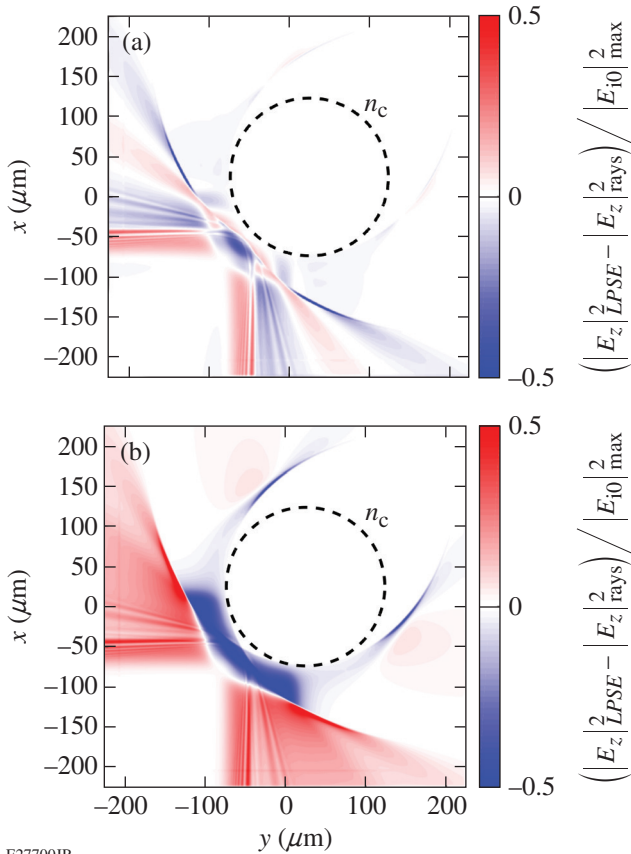

Figure 155.6
(a) Ray- and (b) wave-based simulations of the magnitude of the enveloped electric fields for two beams (injected from the bottom and left) interacting in an azimuthally symmetric plasma. The critical surface is indicated by a dashed line. (c) Lineouts of the fields from *LPSE* (blue) and rays (red). To compare the unperturbed fields, the lineouts are from calculations where CBET was turned off. The location of the caustic is denoted by a vertical dashed black line (where the field amplitude in the ray-based calculation drops to zero).

nearly everywhere in the long-scale-length plasmas encountered in ICF. The difference in field energy between the two calculations is shown in Fig. 155.7(a). Note that while there are significant differences between the two CBET calculations, the ray-based calculation over- and underpredicts the field energy in the scattering region in similar proportion. The differences between the fields are probably due in part to the fact that the laser propagation can be affected by the ponderomotively driven density perturbations in *LPSE* but not in the ray-based calculation. To put Fig. 155.7(a) in context, Fig. 155.7(b) shows the same comparison with CBET turned off in the ray model. This causes the ray-based calculation to dramatically underpredict the amount of scattered light.

Figure 155.6(c) shows a lineout of the fields from the two solutions at one of the caustics in calculations where CBET was turned off ($G_{ijkl} = 0$). The fact that the agreement between

E27700JR

Figure 155.7
The difference in field energy in the ray- and wave-based calculations for (a) CBET turned on and (b) CBET turned off in the ray-based calculation. A Gaussian filter with a 1-μm standard deviation has been applied to smooth out differences resulting from phase mismatches in regions with high-frequency interference.

the solutions is excellent right up to the edge of the ray sheet (vertical dashed black line) suggests that the simple approximation used to calculate the fields at the caustic does not have a significant impact on the accuracy of the global solution. The depicted lineouts were taken relatively far from the center of the caustic to give a stringent test of the ray-based solution; the accuracy of the approximation degrades for increasingly oblique rays.

The limitation of Eq. (4) is depicted in Fig. 155.8, which shows the first sheet of each beam (one shaded gray and one as rays with a black outline) and the Cartesian grid that was used to discretize the ray trajectories. The rays in the beam coming from the left should interact only with the beam coming from the bottom when they are inside the gray region because the field of the beam coming from the bottom vanishes outside that region. Because of the discretization, however, the rays interact wherever they are colored red. In the CGT algorithm, the CBET interaction length in Eq. (5) is allowed to depend on the pump ray such that the gain of a seed ray is limited to only the portion of the grid cell where it is inside the corresponding pump-beam sheet. Accordingly, we introduce a new path length s_{ijkl}, which depends on the indices of the pump ray and appears only in the CBET term but is equal to s_{ij} in grid cells where the beam corresponding to the kth ray does not have a caustic,

$$G_{ijkl} = \frac{s_{ijkl} g_{ijkl} \Delta S_{kl}}{\sqrt{\varepsilon_{\text{eff}}} L_s^{ijkl} \sum_{np \in \mathscr{S}} g_{ijnp}}. \tag{6}$$

The s_{ijkl} is determined by finding the intersections between the seed rays and the sheet boundaries of the pump beams. In 2-D, the sheet boundaries are polygons; in 3-D, the sheet boundaries are closed surfaces that are stored on a triangle mesh. Despite the fact that the CGT correction is spatially localized to the caustic region, it has a large impact on the global solution because of the highly nonlinear nature of Eq. (4). Note that although a Cartesian grid was used here, Eq. (4) does not make any assumptions about the grid, and essentially any gridding scheme will suffer from the same issue (except for an unstructured grid constructed from the sheet boundaries).
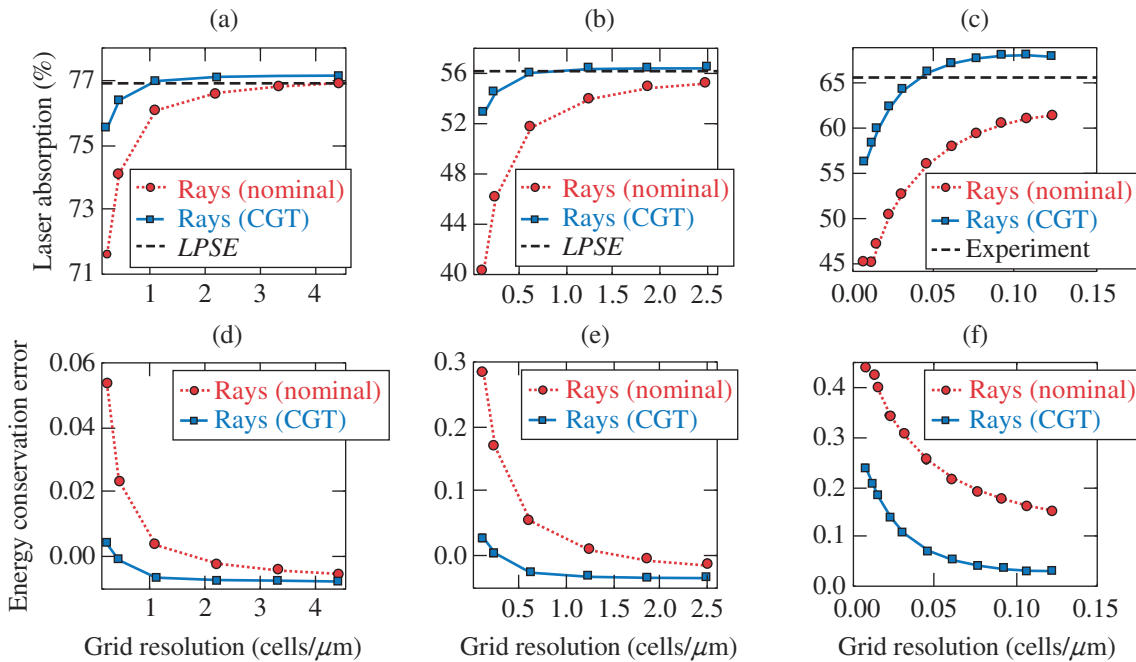
Figures 155.9(a) and 155.9(b) show the laser absorption as a function of the CBET grid resolution using the nominal and CGT ray-based CBET algorithms to two-beam (cf. Fig. 155.6) and 16-beam *LPSE* calculations, respectively. The 16-beam calculations used the same plasma conditions as the two-beam calculations with the beams injected uniformly at 22.5° increments with
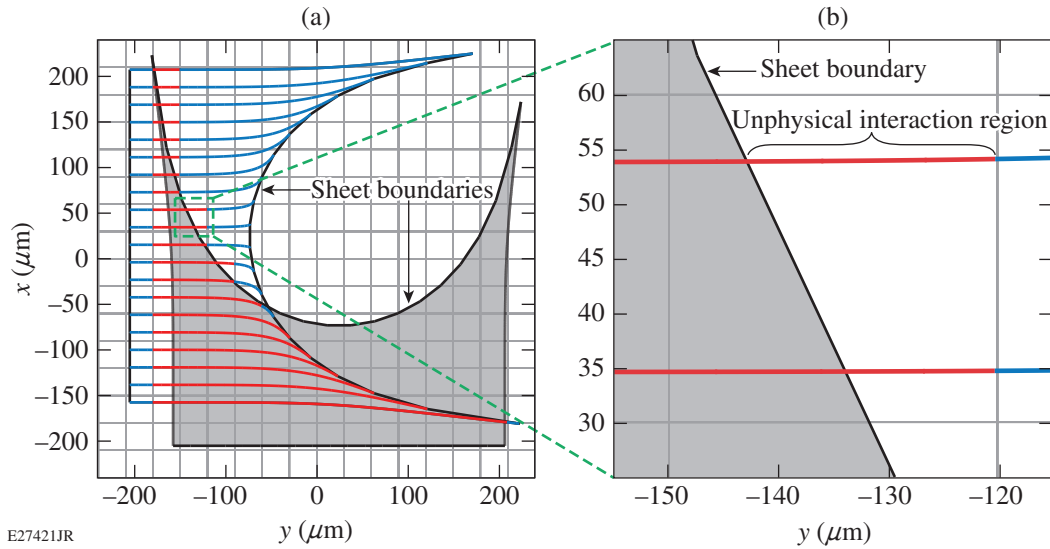
Figure 155.8

(a) The first sheet of the two beams for the configuration shown in Fig. 155.6 overlaid on the Cartesian grid; (b) a close-up of one of the grid cells. The red area of the ray trajectories show where the rays would interact with the beam coming from the bottom without the caustic gain truncation (CGT) correction. Note that finite sheets are shown for illustrative purposes; only the parabolic edge corresponds to a caustic. The other edges of the sheet are chosen such that the intensity is vanishingly small (for the sides) or outside the interaction region (for the injector).

Figure 155.9

[(a)–(c)] The laser absorption and [(d)–(f)] energy conservation error for the nominal (red circles) and CGT (blue squares) ray-trace algorithms as functions of grid resolution for [(a),(d)] 2-D two-beam calculations; [(b),(e)] 2-D 16-beam calculations; and [(c),(f)] 3-D 60-beam calculations. The 2-D calculations are compared to LPSE results and the 3-D calculations are compared to OMEGA results (dashed black lines).

intensities of 4×10^{14} W/cm^2. Both simulations had a significant reduction in laser absorption because of CBET (the absorption without CBET was 96%), and at the highest grid resolutions, the ray-based results were within 0.3% of the *LPSE* results. The nominal and CGT ray-based algorithms converge to the same result in the limit of infinite resolution because the size of the grid cells where the error is introduced in the nominal calculations vanishes. Convergence is achieved much more rapidly using the CGT algorithm, particularly in the 16-beam case (because there are many more caustics). The highest-resolution calculation with the nominal algorithm had an accuracy comparable to the CGT algorithm with an order-of-magnitude-less resolution. The computational cost of solving Eq. (4) is proportional to the number of grid cells, so an order-of-magnitude reduction in resolution represents a large computational savings: a factor of 100 in 2-D and a factor of 1000 in 3-D.

Figure 155.9(c) shows the results of 3-D CBET calculations of the instantaneous laser absorption during the main drive of a 60-beam OMEGA implosion with peak single-beam intensities of 8.8×10^{13} W/cm^2. The plasma profiles were taken from the 1-D radiation-hydrodynamic code *LILAC*.[18] The 3-D calculations included several corrections that are typically included in radiation-hydrodynamic codes (the Langdon effect,[19] the Dewandre effect,[20] and polarization smoothing[16,21]).

As suggested by the difference between the two-beam and 16-beam results in 2-D, the difference between the CGT and nominal algorithms is even more striking in the 3-D 60-beam results. At the highest resolution (4×10^6 grid cells, 7×10^6 rays, and 9×10^9 interactions) that was achievable because of memory constraints, the nominal algorithm was still far from converging with the CGT result. The difference in laser absorption between the CGT calculation at the highest resolution and the experiment was 2.4%.

Figures 155.9(d)–155.9(f) show the energy conservation error in the ray-based solvers (defined as the difference between the incident energy and the sum of the absorbed and scattered energies normalized to the incident energy). It is critical to consider energy conservation when assessing a ray-based CBET algorithm because the underlying discretized equations do not explicitly conserve energy. Away from caustics, they conserve energy in the limit of infinite resolution, but in the presence of caustics, even the converged solutions are nonconserving. The energy conservation error is corrected for in an *ad hoc* manner in radiation-hydrodynamic codes, but there is no consensus as to how such corrections should be implemented. Regardless of

the technique, ray-based CBET results should not be expected to be any more accurate than their uncorrected conservation error because any correction produces a result that is no longer a solution to the original equation. For example, the difference between the nominal ray-trace absorption and the measurement is only 4.2% in the highest-resolution 3-D calculations, but this result is of little value because 15.2% of the energy is unaccounted for and correcting for that could have a large impact on the result. With the CGT algorithm, the conservation error is only 3.4%, which suggests that whatever correction is made to enforce energy conservation will produce a result that is still relatively faithful to Eq. (4).

In summary, a new algorithm was presented for ray-based CBET calculations in the presence of caustics. The CGT algorithm significantly improves accuracy and energy conservation in ray-based CBET calculations and shows excellent agreement with 2-D two- and 16-beam wave-based calculations and a 60-beam OMEGA implosion without the use of artificial multipliers. The increasing discrepancy between the nominal and CGT ray-based CBET algorithms with an increasing number of laser beams emphasizes the importance of a careful treatment of caustics in many-beam laser configurations.

REFERENCES

1. J. Nuckolls *et al.*, Nature **239**, 139 (1972).

2. R. S. Craxton, K. S. Anderson, T. R. Boehly, V. N. Goncharov, D. R. Harding, J. P. Knauer, R. L. McCrory, P. W. McKenty, D. D. Meyerhofer, J. F. Myatt, A. J. Schmitt, J. D. Sethian, R. W. Short, S. Skupsky, W. Theobald, W. L. Kruer, K. Tanaka, R. Betti, T. J. B. Collins, J. A. Delettrez, S. X. Hu, J. A. Marozas, A. V. Maximov, D. T. Michel, P. B. Radha, S. P. Regan, T. C. Sangster, W. Seka, A. A. Solodov, J. M. Soures, C. Stoeckl, and J. D. Zuegel, Phys. Plasmas **22**, 110501 (2015).

3. C. J. Randall, J. R. Albritton, and J. J. Thomson, Phys. Fluids **24**, 1474 (1981).

4. T. R. Boehly, R. S. Craxton, T. H. Hinterman, J. H. Kelly, T. J. Kessler, S. A. Kumpan, S. A. Letzring, R. L. McCrory, S. F. B. Morse, W. Seka, S. Skupsky, J. M. Soures, and C. P. Verdon, Rev. Sci. Instrum. **66**, 508 (1995).

5. I. V. Igumenshchev, W. Seka, D. H. Edgell, D. T. Michel, D. H. Froula, V. N. Goncharov, R. S. Craxton, L. Divol, R. Epstein, R. Follett, J. H.

Kelly, T. Z. Kosc, A. V. Maximov, R. L. McCrory, D. D. Meyerhofer, P. Michel, J. F. Myatt, T. C. Sangster, A. Shvydky, S. Skupsky, and C. Stoeckl, Phys. Plasmas **19**, 056314 (2012).

6. P. Michel *et al*., Phys. Plasmas **16**, 042702 (2009).

7. P. Michel *et al*., Phys. Plasmas **17**, 056305 (2010).

8. V. N. Goncharov, T. C. Sangster, R. Betti, T. R. Boehly, M. J. Bonino, T. J. B. Collins, R. S. Craxton, J. A. Delettrez, D. H. Edgell, R. Epstein, R. K. Follett, C. J. Forrest, D. H. Froula, V. Yu. Glebov, D. R. Harding, R. J. Henchen, S. X. Hu, I. V. Igumenshchev, R. Janezic, J. H. Kelly, T. J. Kessler, T. Z. Kosc, S. J. Loucks, J. A. Marozas, F. J. Marshall, A. V. Maximov, R. L. McCrory, P. W. McKenty, D. D. Meyerhofer, D. T. Michel, J. F. Myatt, R. Nora, P. B. Radha, S. P. Regan, W. Seka, W. T. Shmayda, R. W. Short, A. Shvydky, S. Skupsky, C. Stoeckl, B. Yaakobi, J. A. Frenje, M. Gatu-Johnson, R. D. Petrasso, and D. T. Casey, Phys. Plasmas **21**, 056315 (2014).

9. J. A. Marozas, M. Hohenberger, M. J. Rosenberg, D. Turnbull, T. J. B. Collins, P. B. Radha, P. W. McKenty, J. D. Zuegel, F. J. Marshall, S. P. Regan, T. C. Sangster, W. Seka, E. M. Campbell, V. N. Goncharov, M. W. Bowers, J.-M. G. Di Nicola, G. Erbert, B. J. MacGowan, L. J. Pelz, and S. T. Yang, Phys. Rev. Lett. **120**, 085001 (2018).

10. I. V. Igumenshchev, D. H. Edgell, V. N. Goncharov, J. A. Delettrez, A. V. Maximov, J. F. Myatt, W. Seka, A. Shvydky, S. Skupsky, and C. Stoeckl, Phys. Plasmas **17**, 122708 (2010).

11. D. H. Edgell, R. K. Follett, I. V. Igumenshchev, J. F. Myatt, J. G. Shaw, and D. H. Froula, Phys. Plasmas **24**, 062706 (2017)

12. A. K. Davis, D. Cao, D. T. Michel, M. Hohenberger, D. H. Edgell, R. Epstein, V. N. Goncharov, S. X. Hu, I. V. Igumenshchev, J. A. Marozas, A. V. Maximov, J. F. Myatt, P. B. Radha, S. P. Regan, T. C. Sangster, and D. H. Froula, Phys. Plasmas **23**, 056306 (2016).

13. E. R. Tracy *et al*., *Ray Tracing and Beyond: Phase Space Methods in Plasma Wave Theory* (Cambridge University, Cambridge, England, 2014).

14. W. L. Kruer, *The Physics of Laser Plasma Interactions, Frontiers in Physics*, Vol. 73, edited by D. Pines (Addison-Wesley, Redwood City, CA, 1988).

15. J. D. Huba, NRL Plasma Formulary, Naval Research Laboratory, Washington, DC, Report NRL/PU/6790-94-265 (1994).

16. R. K. Follett, D. H. Edgell, D. H. Froula, V. N. Goncharov, I. V. Igumenshchev, J. G. Shaw, and J. F. Myatt, Phys. Plasma **24**, 103128 (2017).

17. J. F. Myatt, R. K. Follett, J. G. Shaw, D. H. Edgell, D. H. Froula, I. V. Igumenshchev, and V. N. Goncharov, Phys. Plasmas **24**, 056308 (2017).

18. J. Delettrez, R. Epstein, M. C. Richardson, P. A. Jaanimagi, and B. L. Henke, Phys. Rev. A **36**, 3926 (1987).

19. A. B. Langdon, Phys. Rev. Lett. **44**, 575 (1980).)

20. T. Dewandre, J. R. Albritton, and E. A. Williams, Phys. Fluids **24**, 528 (1981).

21. P. Michel *et al*., Phys. Plasmas **20**, 056308 (2013).